Dalton Transactions

PAPER

View Article Online
View Journal | View Issue

Check for updates

Cite this: *Dalton Trans.*, 2023, **52**, 8368

^{57}Fe Mössbauer spectroscopy and high-pressure structural analysis for the mechanism of pressure-induced unique magnetic behaviour in (cation)[$\mathrm{Fe^{II}Fe^{III}(dto)_3}$] (cation = $\mathrm{Ph_4P}$ and $^n\mathrm{PrPh_3P}$; dto = 1,2-dithiooxalato)†

Ryosuke Taniai,[a] Tsubasa Endo,[a] Takuya Kanetomo,*[a] Atsushi Okazawa,[b] Hirokazu Kadobayashi,[c] Saori I. Kawaguchi[c] and Masaya Enomoto*[a]

Received 21st March 2023,
Accepted 15th May 2023

DOI: 10.1039/d3dt00858d

rsc.li/dalton

A mixed-valence iron(II,III) coordination polymer, $\mathrm{(Ph_4P)[Fe^{II}Fe^{III}(dto)_3]}$ (**2**; $\mathrm{Ph_4P}$ = tetraphenylphosphonium, dto = 1,2-dithiooxalato), exhibits a thermal hysteresis loop and a low temperature shift of the ferromagnetic phase transition temperature, with increasing pressure. The latter magnetic behaviour can also be observed in a novel compound $\mathrm{(^nPrPh_3P)[Fe^{II}Fe^{III}(dto)_3]}$ (**3**; $^n\mathrm{PrPh_3P}$ = *n*-propyltriphenylphosphonium). To understand the structural information under pressure, we performed high-pressure powder X-ray diffraction, and the result suggests that there was no structural phase transition for either compound. Considering the ^{57}Fe Mössbauer spectroscopy studies, both **2** and **3** may have a high transition entropy, and this finding is caused by pressure-induced unique magnetic behaviours.

Introduction

Heterobimetallic complexes bridged by a 1,2-dithiooxalato (dto) ligand, $\mathrm{(cation)[M^{II}M^{III}(dto)_3]}$, have a two-dimensional (2-D) honeycomb structure and show a ferromagnetic phase transition.[1–3] The compound $\mathrm{(^nPr_4N)[Fe^{II}Fe^{III}(dto)_3]}$ (**1**; $^n\mathrm{Pr_4N}$ = tetra-*n*-propylammonium) exhibits a ferromagnetic phase-transition temperature (T_c) of 7 K. Interestingly, **1** also shows a charge-transfer phase transition (CTPT) accompanied by electron transfer between the $\mathrm{Fe^{II}}$ and $\mathrm{Fe^{III}}$ sites, as shown in Fig. 1, at the critical temperature (T_{CTPT}) of about 120 K.[4–9] The occurrence of the CTPT in **1** affords two different spin states: (i) a low-temperature phase (LTP) with a low-spin (*ls*) state of $\mathrm{Fe^{II}}$ ($S = 0$) and a high-spin (*hs*) state of $\mathrm{Fe^{III}}$ ($S = 5/2$) and (ii) a high-temperature phase (HTP) with *hs*-$\mathrm{Fe^{II}}$ ($S = 2$) and *ls*-$\mathrm{Fe^{III}}$ ($S = 1/2$) sites. The spin transition due to the CTPT is directly observed from the temperature dependence of magnetic susceptibilities[4–8] and by ^{57}Fe Mössbauer[4] and electron spin resonance spectroscopies.[5] In addition, the CTPT phenomenon can cause various alterations in physical properties such as dielectric responses,[6,7] structural aspects,[8,9] specific heat,[10] muon spin relaxation[11,12] and electric resistivities.[13] Recently, Liu and co-workers reported that a thin film of **1** exhibits ferroelectricity owing to electron hopping between $\mathrm{Fe^{II}}$ and $\mathrm{Fe^{III}}$ sites.[14]

Thermodynamically, the CTPT occurs when $\Delta H_{\mathrm{trs}} = T\Delta S_{\mathrm{trs}}$, derived from $\Delta G = \Delta H - T\Delta S$. For the CTPT of **1**, ΔS_{trs} is dominated by the spin entropy, while ΔH_{trs} is dependent on the intermolecular interaction.[10] To manage T_{CTPT}, the magnitude of ΔS_{trs} and ΔH_{trs} is important; for example, the high-temperature shift of T_{CTPT} needs a smaller ΔS_{trs} or larger ΔH_{trs}. Experimentally, the increase of ΔH_{trs} is more easily achievable for example by applying hydrostatic pressure or by employing

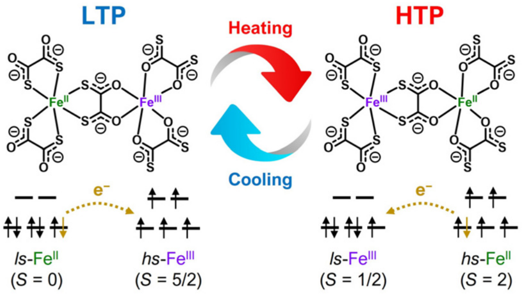

Fig. 1 A charge-transfer phase transition (CTPT) model of **1**.

---

[a] *Tokyo University of Science, 1-3 Kagurazaka, Shinjuku-ku, Tokyo 162-8601, Japan. E-mail: enomoto.masaya@rs.tus.ac.jp*
[b] *Waseda University, 3-4-1 Okubo, Shinjuku-ku, Tokyo 169-8555, Japan*
[c] *Japan Synchrotron Radiation Research Institute (JASRI), SPring-8, Sayo, Hyogo 679-5198, Japan*

† Electronic supplementary information (ESI) available. CCDC 2249917. For ESI and crystallographic data in CIF or other electronic format see DOI: **https://doi.org/10.1039/d3dt00858d**

bulkier cations. In fact, the former approach was applied for **1** and it was found that T_{CTPT} increased up to approximately 200 K with an increase of external pressure from 10^{-4} to 0.9 GPa.[15,16] On the other hand, chemical modification allows the control of internal pressure, and it is well known as "chemical pressure" in spin-crossover (SCO) studies.[17]

Recently, we reported the structural and magnetic studies of $(\mathrm{Ph_4P})[\mathrm{Fe^{II}Fe^{III}(dto)_3}]$ (**2**; $\mathrm{Ph_4P}$ = tetraphenylphosphonium).[18] The bulky and rigid $\mathrm{Ph_4P}$ cation was expected to lead to a large ΔH_{trs} and a high T_{CTPT} compared to **1**, because of the presumable close contact between the $[\mathrm{Fe^{II}Fe^{III}(dto)_3}]$ layer and cations. Compound **2**, however, shows no CTPT behaviour below 300 K. We assumed that the absence of CTPT in **2** is caused by the too large ΔH_{trs}. Indeed, the Curie constant of **2** suggests the spin configuration for the LTP. On the other hand, magnetic measurements under the applied pressure revealed that **2** exhibits a thermal hysteresis loop at around 60 K above 0.76 GPa, indicating that **2** remains in the HTP under ambient pressure. Thus, further studies are required to clarify such a mysterious magnetic behaviour of **2**.

In this study, a new derivative $(^n\mathrm{PrPh_3P})[\mathrm{Fe^{II}Fe^{III}(dto)_3}]$ (**3**; $^n\mathrm{PrPh_3P}$ = *n*-propyltriphenylphosphonium) was synthesized. The *n*-propyl group of the cation can penetrate the honeycomb ring loosely compared to the phenyl group of $\mathrm{Ph_4P}$. The chemical pressure to the intralayer should be smaller than that of **2**, maintaining the interlayer contact. Compound **3** also showed no CTPT behaviour at ambient pressure and the pressure dependence of T_c as in the case of **2**. To explain the pressure-induced unique magnetic behaviour observed in **2** and **3**, we performed high-pressure powder X-ray diffraction (PXRD) on SPring-8 and ambient pressure ^{57}Fe Mössbauer spectroscopy. The former provides the information of the crystal structure at high pressure. The latter can determine the spin and charge states of the Fe ion; specifically, we can obtain the exact spin state for **2** and **3**, which is LTP or HTP.

Experimental

Materials and methods

Compound **3** and $(\mathrm{anilinium})_3[\mathrm{Fe^{III}(dto)_3}](\mathrm{H_2O})$ were prepared by a reported procedure.[18] Compound $^n\mathrm{PrPh_3P}$ bromide was purchased from Sigma-Aldrich. Infrared (IR) spectra were recorded on an FT/IR-4600 (JASCO) spectrometer using a diamond attenuated total reflectance (ATR) method. The spectral data are given as major peaks in wavenumbers (cm^{-1}) and recorded in a spectral window of 4000–400 cm^{-1}. Elemental analyses were conducted using a PerkinElmer Series II CHNS/O 2400 analyser. Powder X-ray diffraction (PXRD) spectra of **2** and **3** were recorded at room temperature (rt) and 1.0×10^{-4} GPa (1 atm) using a Rigaku MiniFlex600 diffractometer (Cu Kα radiation: $\lambda = 1.54184$ Å).

Synthetic procedures

$(^n\mathrm{PrPh_3P})[\mathrm{Fe^{II}Fe^{III}(dto)_3}]$ (**3**) was synthesized as follows. Under an Ar atmosphere, an aqueous solution of $(\mathrm{anilinium})_3[\mathrm{Fe^{III}(dto)_3}]\cdot3\mathrm{H_2O}$ and $\mathrm{FeCl_2\cdot4H_2O}$ 1/1 (10 mmol L^{-1}, 19 mL) was added dropwise to a methanolic solution of $^n\mathrm{PrPh_3P}$ bromide (10 mmol L^{-1}, 19 mL) using a Pasteur pipet with cotton to remove sulphur decomposition products in an ice bath. After the mixture was stirred for 15 minutes, a black precipitate was obtained (40.5 mg, 0.052 mmol, 27%). Anal. calcd for $\mathrm{C_{30}H_{20}Fe_2O_6PS_6}$: C, 41.71; H, 2.85%. Found: C, 41.40; H, 3.05%. Mp. 177 °C (decomp.).

To determine the crystal structure of **3** by single-crystal X-ray diffraction (SCXRD), a single crystal was prepared by a liquid–liquid diffusion method using a $\phi4$ glass tube. A minute amount of ascorbic acid was dissolved in methanol to prevent the oxidation of the iron(II) ion. A methanolic solution of $(\mathrm{anilinium})_3[\mathrm{Fe^{III}(dto)_3}]\cdot3\mathrm{H_2O}$ and $\mathrm{FeCl_2\cdot4H_2O}$ 1/1 (10 mmol L^{-1}, 0.50 mL) was introduced into the glass tube and layered with methanol (0.1 mL) for the purpose of buffering the reaction. A methanolic solution of $^n\mathrm{PrPh_3P}$ bromide (10 mmol L^{-1}, 0.50 mL) was layered on top. After 2 weeks at rt, black hexagonal prismatic crystals were obtained.

Single-crystal X-ray diffraction (SCXRD)

The X-ray diffraction data of **3** were recorded on a Rigaku VariMax Dual diffractometer (Mo Kα radiation: $\lambda = 0.71073$ Å) at 93 K. X-ray data analyses were performed using SHELXT[19] and SHELXL[20] operated with the Olex2 interface.[21] A numerical absorption correction was used. All hydrogen atoms were refined as "riding". The thermal displacement parameters of non-hydrogen atoms were refined anisotropically. We also tried to investigate the fractal dimension distribution of residual electron density as shown in Fig. S1a.†[22] Fig. S1b† shows the distribution of the positive excess electron density around iron ion sites. This charge bias would be induced by the disorder from the valence state of iron sites and linkage isomerization of the ligand. The CCDC number is 2249917.†

Magnetic measurements

The direct current (dc) magnetic susceptibility and magnetization of **3** were measured on a Quantum Design MPMS-XL7AC SQUID magnetometer equipped with a 7 T coil within a temperature range of 2–300 K. The magnetic data were corrected using the diamagnetic blank data of the sample holder measured separately. The diamagnetic contribution of the sample was estimated using Pascal's constant.[23] The dc magnetic susceptibility and magnetization of **3** under high pressures (0.30, 0.38, 0.65 and 1.22 GPa) were measured using a high-pressure cell (HMD01-001-01, Quantum Design). Daphne 7373 (Idemitsu Kosan Co. Ltd) was used as a pressure medium. The applied pressure was determined by a shift in the superconducting transition temperature of tin.

Pressure-induced PXRD

High-pressure PXRD measurements ($\lambda = 0.41277$ Å, 30.0 keV) were carried out on the beamline BL10XU of SPring-8,[24] using a diamond anvil cell with a culet size of 500 µm. The powder sample was placed into a SUS gasket with a hole diameter of 250 µm. Helium was used as a pressure medium, providing a hydrostatic condition. High-pressure powder patterns were recorded on an imaging plate (Rigaku, R-AXIS IV++) detector. The data were converted into one-dimensional profiles (2θ–intensity data) using IP Analyzer software.[25] The XRD profiles were analysed using PDIndexer.[25] Pressures were determined by the ruby fluorescence method.[26] Measurements were performed at rt in compression up to *ca.* 5 GPa.

^{57}Fe Mössbauer spectroscopy

^{57}Fe Mössbauer spectra of **2** and **3** were recorded at 70 K and 200 K on a constant acceleration spectrometer with a γ-ray source of ^{57}Co/Rh in the transmission mode. Measurements were performed using a closed-cycle helium refrigerator (Iwatani Industrial Gases Corp.) and a conventional Mössbauer spectrometer (Topologic Systems). All isomer shifts were obtained relative to α-Fe at rt. The Mössbauer spectra were fitted using the least-squares fitting program MossWinn 4.0.[27]

Results and discussion

Synthesis and characterization

The dto-bridged iron complex, (^{n}PrPh$_3$P)[Fe^{II}Fe^{III}(dto)$_3$] (**3**), was prepared as a black hexagonal prism from (anilinium)$_3$[Fe^{III}(dto)$_3$]·3H$_2$O, Fe^{II}Cl$_2$·4H$_2$O and ^{n}PrPh$_3$P bromide in methanol using a liquid–liquid diffusion method. In addition, the powder sample of **3** was obtained by simply mixing the above starting materials to measure the magnetic properties and characterized using elemental and powder X-ray crystallographic analyses (for details, see below).

Crystal structures

The crystal structure of **3** was determined by SCXRD at 93 K, as shown in Fig. S2† and Table 1. It was observed to be isomorphic with **2**.[18] The iron centres are bridged by the dto ligand, and two coordination geometries of {FeO$_6$} and {FeS$_6$} were constructed, as shown in Fig. S2a.† The anionic [Fe^{II}Fe^{III}(dto)$_3$] unit forms a 2-D honeycomb structure in the *ab* plane. The shortest Fe1···Fe2 distance is 5.820 Å. The anion layer stacks as an eclipsed form along the *c*-axis. The ^{n}PrPh$_3$P counter cation is present in the void space of the anion layer and exhibited two disordered configurations, which were placed above and below the anion layer, as shown in Fig. S2b.† The *n*-propyl chain of the cation penetrates a hexagonal hole of the honeycomb layer with three disorder conformations according to the three-fold axis.

The structural parameters for **3** and **2** as a reference are summarized in Table 2. For **3**, the mean values of the coordination bond lengths (d_{mean}) of the Fe–O and Fe–S bonds are 2.134(7) and 2.274(3) Å, respectively. The coordination polyhedra of O$_6$ and S$_6$ are ascribed to an approximately octahedral geometry (O_h). As observed in the O_h distortion parameters (Σ and Θ),[29] the {FeO$_6$} environment is largely distorted, whereas that of {FeS$_6$} is close to the regular octahedron. Compared with **2**, both {FeO$_6$} and {FeS$_6$} coordination environments of **3** are closer to the solid O_h geometry.

We investigated the intermolecular contacts between the cation and anion layers in **3**, as shown in Fig. 2a. For the inserted *n*-propyl moiety, the closest C10···S1^a and C10···O1^a distances are 3.81(7) and 3.68(5) Å, respectively. These values were larger than the sum of van der Waals (vdW) radii (C/S: 3.50 Å; C/O: 3.22 Å)[30] and those of **2** of 3.283(18) Å (C···S) and 3.37(3) Å (C···O).[18] In addition, as shown in Fig. 2b, for three phenyl rings of the cation located between the layers, the nearest C6···S2^b and C7···O2^c distances were 3.62(3) and 3.28(3) Å, respectively, which were slightly larger than the sum of vdW radii. On the other hand, these reproduce the values of **2** of 3.60(3) Å (C···S) and 3.27(3) Å (C···O). Therefore, these results indicate that the intralayer and interlayer contacts are smaller and unchanged, respectively, compared to **2**. In other words, the ΔH_{trs} value of **3** is smaller than that of **2** due to the clearance between the honeycomb structure and the penetrating *n*-propyl group of the cation.

Magnetic measurements

The $\chi_{\mathrm{m}}T$ *vs.* T plots for **3** upon heating (red open circles) and cooling (blue filled circles) processes from 2 to 300 K under

Table 1 Selected cell parameters for **2** and **3**

Compound	**3**	**2**^{c}
Formula	C$_{27}$H$_{22}$Fe$_2$O$_6$S$_6$P	C$_{30}$H$_{20}$Fe$_2$O$_6$PS$_6$
Formula weight	777.48	811.49
T/K	93	93
Crystal system	Hexagonal	Hexagonal
Space group	$P6_3$	$P6_3$
a/Å	10.0805(4)	10.0960(3)
c/Å	17.8516(10)	17.9325(7)
V/Å^3	1570.98(15)	1582.96(11)
Z	2	2
d_{calc}/g cm^{-3}	1.644	1.703
μ(Mo Kα)/mm^{-1}	1.407	1.407
$R(F)^a$ ($I > 2\sigma(I)$)	0.0679	0.0680
$R_{\mathrm{w}}(F^2)^b$ (all data)	0.1804	0.1685
Goodness-of-fit	1.150	1.189
No. of unique reflns	2131	2319

[a] $R = \sum||F_{\mathrm{o}}| - |F_{\mathrm{c}}||/\sum|F_{\mathrm{o}}|$. [b] $R_{\mathrm{w}} = [\sum w|F_{\mathrm{o}}{}^2 - F_{\mathrm{c}}{}^2|^2/\sum w(F_{\mathrm{o}}{}^2)^2]^{1/2}$. [c] Ref. 18.

Table 2 Structural parameters for **3** in addition to **1** and **2** as a reference

Compound	**3**	**2**^{a}	**1**^{a,b}	
T/K	93	93	88	140
{O$_6$}				
d_{mean} (Fe–O)/Å	2.134(7)	2.131(7)	2.139(5)	2.141(6)
Σ/°	75.69	83.50	68.71	70.58
Θ/°	240.36	260.04	218.94	224.29
Octahedron (O_h)^c	1.178	1.482	0.998	1.057
Trigonal prism (D_{3h})^c	13.241	12.238	13.220	13.102
{S$_6$}				
d_{mean} (Fe–S)/Å	2.274(3)	2.272(3)	2.281(3)	2.289(4)
Σ/°	8.256	16.68	27.31	28.15
Θ/°	28.06	58.85	97.60	100.48
Octahedron (O_h)^c	0.015	0.061	0.170	0.179
Trigonal prism (D_{3h})^c	15.945	15.035	13.950	13.917

[a] Ref. 18. [b] Ref. 9. [c] SHAPE software.[28]

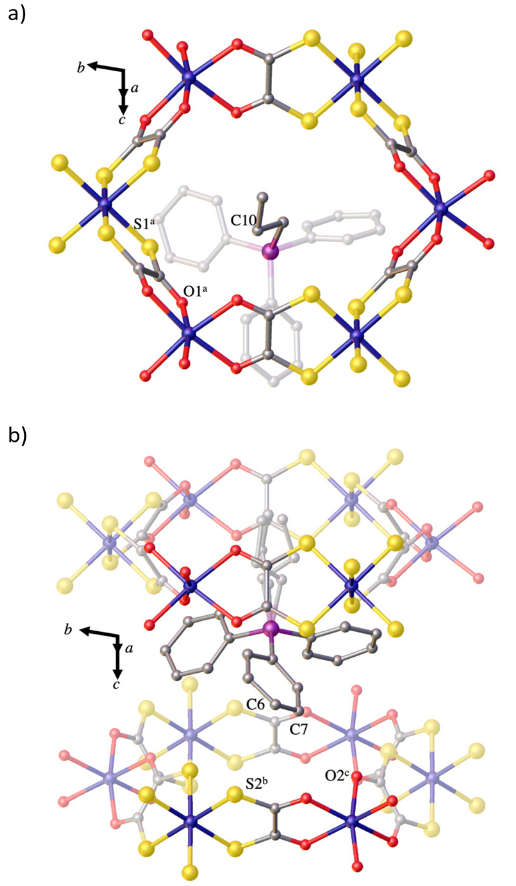

Fig. 2 (a) Coordination environment of O_6 and S_6 atoms for the two Fe ions in **3**. Colour codes: gray, red, yellow, purple and navy represent C, O, S, P, and Fe atoms, respectively. A 2-D honeycomb layer in the *ab* plane is shown. (b) Layered structure along the *c* axis. One side of two disordered configurations is shown in the $^{n}PrPh_3P$ position. Symmetry codes: (a) 1+*x*, 1+*y*, +*z*; (b) 1+*y*, 1−*x*+*y*, 1/2+*z*; (c) 1−*y*+*x*, +*x*, 1/2+*z*.

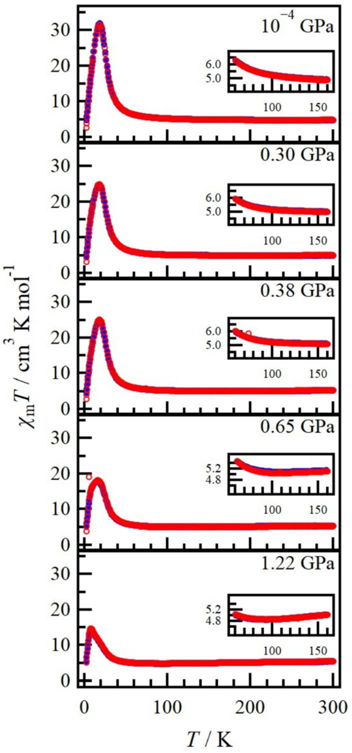

Fig. 3 Temperature dependence of the product, χ_mT, measured at 5 kOe for **3**. Red open and blue filled circles represent the heating and cooling processes, respectively, under 1.0 × 10^{-4}, 0.30, 0.38, 0.65 and 1.22 GPa. The inset shows a magnified plot.

pressures of 1.0 × 10^{-4}, 0.30, 0.38, 0.65 and 1.22 GPa are shown in Fig. 3. First, under 1.0 × 10^{-4} GPa, the data on a cooling process in 100–300 K were analysed using the Curie–Weiss equation: $\chi = C/(T - \theta)$, in which C and θ are Curie and Weiss constants, respectively. The best fit was obtained with C = 4.661(5) cm^3 K mol^{-1} and θ = +9.3(2) K (a solid line in Fig. S3†). The experimental C value is close to that of **2** of 4.466(1) cm^3 K mol^{-1} and larger than those of the HTP state in $((n\text{-}C_nH_{2n+1})_4N)[Fe^{II}Fe^{III}(dto)_3]$, in which n = 3 (**1**; 3.90 cm^3 K mol^{-1}), 4 (**4**; 3.56 cm^3 K mol^{-1}), 5 (**5**; 3.88 cm^3 K mol^{-1}) and 6 (**6**; 3.52 cm^3 K mol^{-1}).[5] In the previous work,[18] we assumed that the C value reproduces the theoretical value of 4.38 cm^3 K mol^{-1} derived from *ls*-Fe^{II} (S = 0) and *hs*-Fe^{III} (g = 2 and S = 5/2) ions corresponding to the LTP. However, the results of ^{57}Fe Mössbauer spectroscopy (for details, see below) indicate that the Fe^{II} and Fe^{III} sites in both **2** and **3** are in *hs* (S = 2) and *ls* (S = 1/2) states, respectively; specifically, the spin state of both compounds is the HTP. For the HTP, the expected C value (fixed as g = 2) is 3.38 cm^3 K mol^{-1}, and the value is smaller than the experimental C values. According to the structural analyses, the $\{Fe^{II}O_6\}$ site was a distorted O_h symmetry; it can exhibit a large g value (> 2).[31] To fit the experimental C values of **2** and **3**, the g values of $\{Fe^{II}O_6\}$ were estimated to be 2.34 and 2.39, respectively. In this case, we fixed the g-value of *ls*-Fe(III) as 2.00 since the regular octahedral ligand field of $\{Fe^{III}S_6\}$ tends to give that value.

Compound **2** exhibited a pressure-induced thermal hysteresis in χ_mT *vs.* T, whereas **3** showed no clear CTPT under the applied pressures, as shown in the insets of Fig. 3. Note that the thermal hysteresis derived from the CTPT may be hidden by the measurement error because the change of the χ_mT values during the CTPT is small.[4,18] For this matter, it may be observed by high-pressure dielectric measurements.[6,7] The maximum χ_mT value under 1.0 × 10^{-4} GPa observed at 20 K was shifted to the low-temperature side with increasing pressure and reached 8 K at 1.22 GPa. The results for the T-dependence of field-cooled (FCM, red marker), zero-field cooled (ZFCM, blue marker) and remnant (RM, green marker) magnetizations under 1.0 × 10^{-4}, 0.30, 0.38, 0.65 and 1.22 GPa are shown in Fig. 4. Compound **3** exhibited a ferromagnetic phase transition under all pressures with T_c values from 1.0 × 10^{-4} to 1.22 GPa of 11.2, 10.2, 10.6, 9.4 and 6.5 K, respectively. The T_c value was found to shift towards lower temperatures with increasing pressure. This finding also reproduces the trend of T_c for **2**, which is from 9.8 K (1.0 × 10^{-4}) to 3.6 K (1.35 GPa).[18]

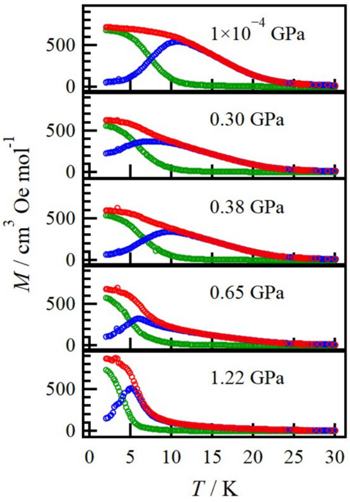

Fig. 4 Temperature dependence of FCM (red), ZFCM (blue) and RM (green) measured at 30 and 0 Oe for **3** under 1.0 × 10^{-4}, 0.30, 0.38, 0.65 and 1.22 GPa.

^{57}Fe Mössbauer spectroscopy

To clarify the spin states of the Fe sites, ^{57}Fe Mössbauer spectroscopy was performed for **2** and **3** at 70 and 200 K under ambient pressure as shown in Fig. 5. The Mössbauer parameters are listed in Table 3. There is no remarkable spectral change varied with temperature between 70 K and 200 K in both **2** and **3**, indicating no CTPT behaviour. In the spectra of **3**, two main doublets were observed (yellow and green lines) with about 50% fractions. The wide doublet (green) has an isomer shift (δ) of 1.054(6) mm s^{-1} and a quadrupole splitting (ΔE_Q) of 1.79(2) mm s^{-1} at 200 K corresponding to *hs*-Fe^{II} (S = 2).[32–34] On the other hand, the narrow-splitting doublet (yellow) can be assigned to *ls*-Fe^{III} (S = 1/2) because the obtained parameters (δ = 0.207(8) mm s^{-1} and ΔE_Q = 0.67(1) mm s^{-1}) are reasonable for those found in related dto-bridged iron compounds.[35,36] Thus, the spin state of **3** corresponds to the HTP. A minor doublet (blue) was also found as a fraction of less than 10% in the spectra of **3**, which is derived from a linkage isomer such as FeO_4S_2 with the *hs*-Fe^{II} state.[37,38]

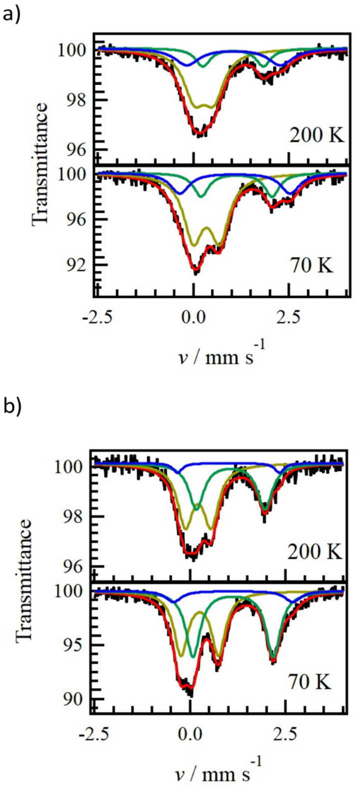

Fig. 5 ^{57}Fe Mössbauer spectra of (a) **2** and (b) **3** at 70 and 200 K (black lines). Yellow doublets represent the *ls*-Fe^{III} ion and the blue and green lines represent the *hs*-Fe^{II} ion. Red lines are the sum of the above three simulated lines.

Table 3 Mössbauer parameters of **2** and **3** at 70 and 200 K

T/K	Spin state	Area/ %	δ^a/ mm s^{-1}	$\Delta E_Q{}^b$/ mm s^{-1}	Line width^c/ mm s^{-1}
Compound 2					
70	***ls*-Fe(III)**	61.48	0.333(6)	0.69(1)	0.61(2)
	***hs*-Fe(II)_A**	18.14	1.12(1)	1.85(3)	0.47(4)
	***hs*-Fe(II)_B**	20.39	1.08(1)	2.88(5)	0.61(6)
200	***ls*-Fe(III)**	57.71	0.27(1)	0.50(2)	0.67(3)
	***hs*-Fe(II)_A**	16.53	1.03(1)	1.58(5)	0.47(9)
	***hs*-Fe(II)_B**	25.75	1.05(3)	2.4(1)	0.8(1)
Compound 3					
70	***ls*-Fe(III)**	44.18	0.247(5)	0.979(9)	0.45(1)
	***hs*-Fe(II)_A**	47.06	1.121(4)	2.10(1)	0.45(2)
	***hs*-Fe(II)_B**	8.77	1.12(2)	3.11(7)	0.49(10)
200	***ls*-Fe(III)**	54.38	0.207(8)	0.67(1)	0.49(2)
	***hs*-Fe(II)_A**	40.31	1.054(6)	1.79(2)	0.47(3)
	***hs*-Fe(II)_B**	5.31	1.00(3)	2.66(6)	0.3(1)

[a] δ [mm s^{-1}] = isomer shift. [b] ΔE_Q [mm s^{-1}] = quadrupole splitting. [c] Full width at the half-maximum (FWHM) of the line.

The spectra of **2** showed three doublets with the parameters similar to those of **3**. The presence of *hs*-Fe^{II} signals confirms that **2** lies in the HTP. However, the intensities of two *hs*-Fe^{II} doublets (green and blue) are comparable to each other, indicating that linkage isomerization of the ligand is more frequent than in **3**. The linkage isomerisation is also found in **1** and Kagesawa and co-workers reported that the ratio depends on the synthetic conditions, *i.e.* the solvent and the reaction temperature.[38] Although the synthetic approach for powders **2** and **3** was the same, there was a difference in the yields of 79 and 27%, respectively. Here, **2** has many more intra- and inter-layer contacts than **3**, according to the SCXRD studies. This finding suggests that the formation of the crystal structure is more rapid, resulting in a high yield. On the other hand, the rapid crystal structure formation may tend to provide the structural domain having a linkage isomer. Fortunately, the CTPT behaviour is independent on the ratio of the linkage isomer.[37]

Pressure-dependent PXRD

We carried out high-pressure PXRD measurements for **2** and **3** at rt in SPring-8 under 0.46(3)–5.26(8) GPa and 0.32(2)–5.13(9) GPa, respectively. The experimental XRD patterns for **2** and **3**

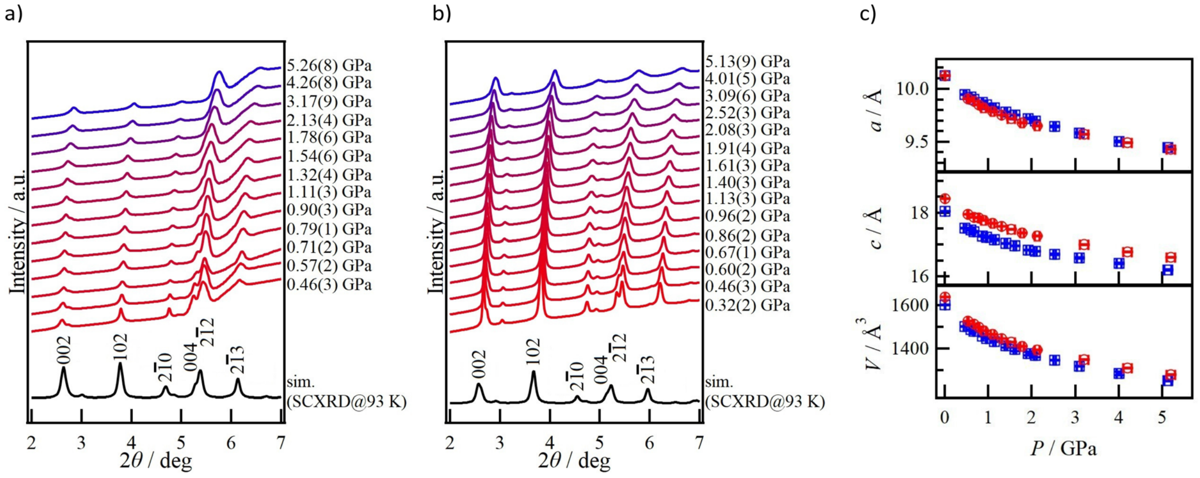

Fig. 6 Variable-pressure PXRD measurements for (a) **2** and (b) **3** in the range of 1.0×10^{-4} (1 atm)–5.26 and 1.0×10^{-4} (1 atm)–5.13 GPa, respectively. Simulation curves (black line) were derived from the SCXRD results at 93 K. (c) Pressure dependence of cell parameters (top) *a*, (middle) *c* and (bottom) *V* for **2** (red circles) and **3** (blue squares). The black filled circle and square represent the simulation derived from the SCXRD results at 93 K for **2** and **3**, respectively.

are shown in Fig. 6a and b, respectively. Also, the powder patterns simulated from the SCXRD results at 93 K are displayed (black lines). Moreover, the experimental results of powder patterns for **2** and **3** were similar to that of these SCXRD results at 93 K, judging from the previous[18] and this work in Fig. S4.† We assumed that **2** exhibit the pressure-induced thermal hysteresis and the shift of T_c are caused by the structural phase transition under high pressure.[18] If there is a structural transition such as a change from eclipsed to staggered forms, the XRD patterns should show a discontinuous change.[39–41] However, both compounds showed that all peaks gradually shifted to a higher angle and broadened with increasing pressure from 0.46 to 5.26 GPa. The (004) peak was clearly visible at low pressure, but gradually integrated with the neighbouring peak of (2$\bar{1}$2). The XRD patterns under high pressure indicate typical shrinking of the unit cell owing to the applied pressure rather than the structural transition.

To understand the cell constants at each pressure, the XRD profiles were analysed using PDIndexer.[25] The results are summarized in Tables S1 and S2† and Fig. 6c. The pressure dependences of *a* constant for **2** and **3** were similar. On the other hand, the *c* constant of **3** decreased more significantly with the applied pressure than that of **2**. The compression along the *c*-axis (the stacking direction) depends on the ease of movement of the inserted moieties in the counter cation; specifically, the weaker intralayer contact favours the strong pressure-dependence of the *c* constant. In this study, **3** has weaker intralayer contacts than **2**, supporting the results of high-pressure PXRD measurements.

Discussion

Compound **2** exhibited a pressure-induced thermal hysteresis in the temperature dependence of magnetic moment and a low-temperature shift of T_c.[18] Analogue **3** also exhibited the latter behaviour. These magnetic behaviours could be related to the CTPT, and in the previous work, we assumed that **2** shows the LTP below 300 K owing to the Curie constant estimated by the magnetic measurement. For such a situation, the LTP state gives T_{CTPT} > 300 K and a large ΔH_{trs} such as the blue line in Fig. 7a. The pressure-induced thermal hysteresis loop observed in **2** was explained by the structural phase transition with a large drop of ΔH_{trs} triggered by the applied pressure, the green line in Fig. 7a. However, in this study, the results of ^{57}Mössbauer and high-pressure XRD spectroscopy studies for **2** and **3** revealed the spin state of the HTP below 300 K at ambient pressure and no structural phase transition triggered by the applied pressure. These findings imply the small ΔH_{trs} and/or large ΔS_{trs}, compared with **1**. The former

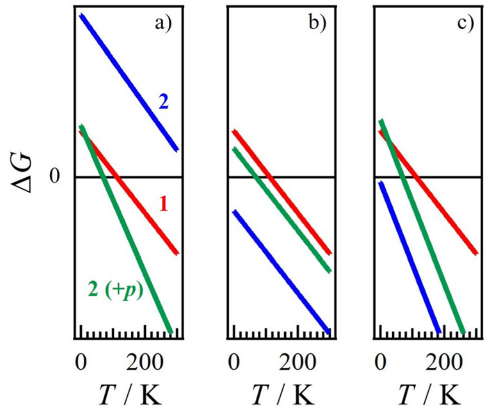

Fig. 7 Schematic drawing of Δ*G* *vs.* the *T* diagram for the pressure-induced CTPT behaviour of **2** according to a mechanism proposed (a) in the previous work (ref. 18) and (b and c) in this work. Red, blue and green solid lines stand for **1** at 1 atm as the reference and **2** at 1 atm and the applied pressure, respectively.

can be illustrated as shown in Fig. 7b. The ΔS_{trs} value, giving the tilt of ΔG, is the same as for **1**. For the enthalpy, we have assumed that the intermolecular contact is the key factor. Compound **2** had more contact than **1**, indicating a large ΔH_{trs}. However, the experimental result in this paper suggests a small ΔH_{trs} value in **2** and **3**, and thus we should assume that there are two possibilities: (i) the lattice energy in the eclipsed stacking manner in **2** and **3** is smaller than that of the staggered one in **1** and/or (ii) the coordination environment around the iron sites for **2** and **3** favours the HTP state than that of **1**.

On the other hand, if the increase of ΔS_{trs} is also taken into account, the decrease of ΔH_{trs} can be reduced, as shown in Fig. 7c. For the CTPT behaviour, the transition entropy ΔS_{trs} is composed of the change in spin multiplicity, orbital angular momentum and vibrational contribution. First, the change in the spin multiplicity can be estimated to be $R\ln(10/6) = 4.25$ J K^{-1} mol^{-1}, where R is the gas constant. This value should be independent of cations and crystal structures, and thus it is not relevant to the contribution of the above larger ΔS_{trs}. Next, the vibrational contribution is caused by the difference in the structures of the HTP and LTP states. Itoi and co-workers reported that there was almost no difference in the crystal structures of two phases for **1**; namely, the vibrational contribution is small.[9] On the other hand, **2** and **3** could show a large difference in the structures of the HTP and LTP states, because we have no structural data for the LTP of both compounds. In this case, no CTPT behaviour could be observed due to the vibrational contribution. Finally, the change in the orbital angular momentum varies by the coordination environment around the iron sites. According to ref. [10], when the ligand-field symmetry remains O_h through the CTPT, the change in the orbital angular momentum is estimated to be $\Delta S = R\ln\{(3 \times 3)/(1 \times 1)\} = 18.27$ J K^{-1} mol^{-1} from the HTP (*hs*-Fe$^{\text{II}}$, $^5T_{2g}$; *ls*-Fe$^{\text{III}}$, $^2T_{2g}$) and the LTP (*ls*-Fe$^{\text{II}}$, $^1A_{1g}$; *hs*-Fe$^{\text{III}}$, $^6A_{1g}$). If there is a slightly distorted O_h symmetry to the trigonal antiprism (D_{3d}), the ΔS value becomes $R\ln\{(1 \times 2)/(1 \times 1)\} = 5.76$ J K^{-1} mol^{-1} from the HTP (*hs*-Fe$^{\text{II}}$, $^5A_1$; *ls*-Fe$^{\text{III}}$, ^2E) and the LTP (*ls*-Fe$^{\text{II}}$, $^1A_{1g}$; *hs*-Fe$^{\text{III}}$, $^6A_{1g}$). For both Fe sites of **1**, there could be a lower symmetry than the D_{3d} one, indicating a small contribution to ΔS_{trs}. Here, two iron sites, $\{FeO_6\}$ and $\{FeS_6\}$, for **2** and **3** exhibited the O_h symmetry, and in particular, the $\{FeS_6\}$ site is almost a regular octahedron. The structural results allow **2** and **3** to achieve the contribution of the change in orbital momentum of $\Delta S = R\ln\{(1 \times 3)/(1 \times 1)\} = 9.13$ J K^{-1} mol^{-1}, which could be larger than that of **1**. Therefore, the large ΔS_{trs} value, giving the HTP state with no CTPT (Fig. 7c), could be generated by the vibrational and/or orbital angular momentum contributions.

High-pressure environments allow crystalline compounds to give two conditions: (i) the enhancement of intermolecular contacts and/or (ii) a distorted coordination environment around the Fe sites. These conditions give a larger ΔH_{trs} and a smaller ΔS_{trs}, respectively. It is well known that the SCO behaviour is shifted to the high-temperature side on increasing the pressure.[17] In fact, for the dto-bridged bimetallic compounds, **1** exhibits the high-temperature shift of T_{CTPT} under the applied pressure, whereas the T_c value is almost independent of the pressure.[15] On the other hand, the tetra-*n*-pentylammonium derivative **5**, which shows the HTP below 300 K with no CTPT at 1 atm, exhibit a thermal hysteresis in the temperature dependence of magnetic moment above 0.55 GPa.[42] In addition, the T_c of **5** is shifted from 18 K to 7 K triggered by applying a high pressure. The magnetic studies of **5** are consistent with those of **2** and **3**. Compound **5** may have an isomorphic structure to **1**, although the details of structural information are unfortunately unclear.[5] Therefore, **2** with the large ΔS_{trs} could exhibit the CTPT behaviour induced by the applied pressure, as shown in Fig. 7c. On the other hand, although **3** exhibited a similar structure to **2** and a low-temperature shift of T_c, there was no clear evidence of CTPT in the pressure-induced magnetic measurement. To confirm whether or not CTPT occurs, different approaches, such as high-pressure dielectric and SCXRD measurements, should be carried out in the future.

Conclusions

Compound **2** showed pressure-induced thermal hysteresis and the low-temperature shift of T_c, which could be related to the CTPT phenomenon. In this study, we investigated the exact spin state and the crystal structure under high pressure to understand the above unique magnetic behaviour. The result of ^{57}Fe Mössbauer spectroscopy for **2** suggested the HTP state with no CTPT. In addition, high-pressure PXRD revealed that there was no structural phase transition triggered by the applied pressure. These findings were supported by the results of the novel derivative **3**. The HTP state with no CTPT in **2** and **3** suggests that the ΔS_{trs} is larger than that of **1**, owing to the vibrational and/or orbital angular momentum contributions. If high-pressure SCXRD measurement, measured below T_{CTPT}, is performed, we could determine the major component of the large transition entropy.

Conflicts of interest

There are no conflicts to declare.

Acknowledgements

The crystallography work for **3** was conducted at the Advanced Characterization Nanotechnology Platform of the University of Tokyo, supported by the "Nanotechnology Platform" of the Ministry of Education, Culture, Sports, Science and Technology (MEXT), Japan. The high-pressure PXRD measurements of **2** and **3** were performed at BL10XU on SPring-8 (Proposal Number 2022A1224).

References

1 H. Ōkawa, M. Mitsumi, M. Ohba, M. Kodera and N. Matsumoto, *Bull. Chem. Soc. Jpn.*, 1994, **67**, 2139–2144.

2 Y. Ono, M. Okubo and N. Kojima, *Solid State Commun.*, 2003, **126**, 291–296.

3 J. M. Bradley, S. G. Carling, D. Visser, P. Day, D. Hautot and G. J. Long, *Inorg. Chem.*, 2003, **42**, 986–996.

4 N. Kojima, W. Aoki, M. Seto, Y. Kobayashi and Yu. Maeda, *Synth. Met.*, 2001, **121**, 1796–1797.

5 M. Itoi, Y. Ono, N. Kojima, K. Kato, K. Osaka and M. Takata, *Eur. J. Inorg. Chem.*, 2006, **2006**, 1198–1207.

6 H. Ida, A. Okazawa, N. Kojima, R. Shimizu, Y. Yamada and M. Enomoto, *Inorg. Chem.*, 2012, **51**, 8989–8996.

7 M. Enomoto, H. Ida, A. Okazawa and N. Kojima, *Crystals*, 2018, **8**, 446.

8 M. Itoi, A. Taira, M. Enomoto, N. Matsushita, N. Kojima, Y. Kobayashi, K. Asai, K. Koyama, T. Nakano, Y. Uwatoko and J. Yamaura, *Solid State Commun.*, 2004, **130**, 415–420.

9 M. Itoi, A. Okazawa, J. Yamaura, S. Maki, T. Komatsu, I. Maurin, E. Codjovi, K. Boukheddaden and N. Kojima, *Inorg. Chem.*, 2018, **57**, 13728–13738.

10 T. Nakamoto, Y. Miyazaki, M. Itoi, Y. Ono, N. Kojima and M. Sorai, *Angew. Chem.*, 2001, **113**, 4852–4855.

11 M. Enomoto, M. Itoi, Y. Ono, M. Okubo and N. Kojima, *Synth. Met.*, 2003, **137**, 1231–1232.

12 N. Kida, M. Enomoto, I. Watanabe, T. Suzuki and N. Kojima, *Phys. Rev. B: Condens. Matter Mater. Phys.*, 2008, **77**, 144427.

13 M. Enomoto, N. Kida, I. Watanabe, T. Suzuki and N. Kojima, *Physica B: Condens. Matter*, 2009, **404**, 642–644.

14 X. Liu, B. Wang, X. Huang, X. Dong, Y. Ren, H. Zhao, L. Long and L. Zheng, *J. Am. Chem. Soc.*, 2021, **143**, 5779–5785.

15 Y. Kobayashi, M. Itoi, N. Kojima and K. Asai, *J. Phys. Soc. Jpn.*, 2002, **71**, 3016–3020.

16 M. Itoi, N. Kida, L. Chin, M. Koeda, N. Kojima, M. Hedo, Y. Uwatoko, Y. Kobayashi, K. Asai, Y. Ohishi and M. Takta, *J. Phys. Soc. Jpn.*, 2007, **76**, 190–191.

17 *Spin Crossover in Transition Metal Compounds I*, ed. P. Gütlich and H. A. Goodwin, Springer, Berlin, Heidelberg, 2004, vol. 233.

18 K. Nomura, T. Kanetomo and M. Enomoto, *Cryst. Growth Des.*, 2022, **22**, 2139–2145.

19 G. M. Sheldrick, *Acta Crystallogr., Sect. A: Found. Adv.*, 2015, **71**, 3–8.

20 G. M. Sheldrick, *Acta Crystallogr., Sect. C: Struct. Chem.*, 2015, **71**, 3–8.

21 L. J. Bourhis, O. V. Dolomanov, R. J. Gildea, J. A. K. Howard and H. Puschmann, *Acta Crystallogr., Sect. A: Found. Adv.*, 2015, **71**, 59–75.

22 K. Meindl and J. Henn, *Acta Crystallogr., Sect. A: Found. Adv.*, 2008, **64**, 404–418.

23 O. Kahn, *Molecular Magnetism*, VCH-Verlag, Weinheim, New York, 1993.

24 N. Hirao, S. I. Kawaguchi, K. Hirose, K. Shimizu, E. Ohtani and Y. Ohishi, *Matter Radiat. Extremes*, 2020, **5**, 018403.

25 Y. Seto, D. Hamane, T. Nagai and N. Sata, *Rev. High Pressure Sci. Technol.*, 2010, **20**, 269–276.

26 C.-S. Zha, H. Mao and R. J. Hemley, *Proc. Natl. Acad. Sci. U. S. A.*, 2000, **97**, 13494–13499.

27 Z. Klencsár, E. Kuzmann and A. Vértes, *J. Radioanal. Nucl. Chem.*, 1996, **210**, 105–118.

28 M. Lluncll, D. Casanova, J. Circra, J. M. Bofill, P. Alcmany, S. Alvarez, M. Pinsky and D. Avnir, *SHAPE, v2.1*, University of Barcelona and The Hebrew University of Jerusalem, 2005.

29 C. A. Kilner and M. A. Halcrow, *Dalton Trans.*, 2010, **39**, 9008–9012.

30 A. Bondi, *J. Phys. Chem.*, 1964, **68**, 441–451.

31 B.-L. Fei, R. Clérac, C. E. Anson and A. K. Powell, *Dalton Trans.*, 2005, 1381–1386.

32 T. Birchall and K. M. Tun, *Inorg. Chem.*, 1976, **15**, 376–380.

33 R. M. Golding, K. F. Mok and J. F. Duncan, *Inorg. Chem.*, 1966, **5**, 774–778.

34 C. D. Burbridge, D. M. L. Goodgame and M. Goodgame, *J. Chem. Soc. A*, 1967, 349–352.

35 S. Iijima, T. Katsura, H. Tamaki, M. Mitsumi, N. Matsumoto and H. Ōkawa, *Mol. Cryst. Liq. Cryst.*, 1993, **233**, 263–268.

36 A. Okazawa, J. Yoshida, N. Kida, I. Kashima, W. Murata, M. Enomoto and N. Kojima, *Hyperfine Interact.*, 2014, **226**, 351–357.

37 N. Kojima, Y. Ono, K. Kobayashi and M. Seto, *Hyperfine Interact.*, 2004, **156/157**, 175–179.

38 K. Kagesawa, N. Kida, Y. Ono, M. Enomoto and N. Kojima, *J. Phys.: Conf. Ser.*, 2010, **217**, 012034.

39 Z. Yang, H. Chen, S. Wang, W. Guo, T. Wang, X. Suo, D. Jiang, X. Zhu, I. Popovs and S. Dai, *J. Am. Chem. Soc.*, 2020, **142**, 6856–6860.

40 B. Lukose, A. Kuc and T. Heine, *Chem. – Eur. J.*, 2011, **17**, 2388–2392.

41 Y. Du, D. Calabro, B. Wooler, Q. Li, S. Cundy, P. Kamakoti, D. Colmyer, K. Mao and P. Ravikovitch, *J. Phys. Chem. C*, 2014, **118**, 399–407.

42 Y. Kobayashi, M. Itoi, K. Kojima and K. Asai, *J. Magn. Magn. Mater.*, 2004, **272–276**, 1091–1092.